The Astronomical Journal, 161:284 (13pp), 2021 June https://doi.org/10.3847/1538-3881/abf3c3

ARES.* V. No Evidence For Molecular Absorption in the HST WFC3 Spectrum of GJ 1132 b

Lorenzo V. Mugnai[1], Darius Modirrousta-Galian[2,3], Billy Edwards[4], Quentin Changeat[4], Jeroen Bouwman[5], Giuseppe Morello[2,6], Ahmed Al-Refaie[4], Robin Baeyens[7], Michelle Fabienne Bieger[8], Doriann Blain[9], Amélie Gressier[9,10], Gloria Guilluy[11,12], Yassin Jaziri[13], Flavien Kiefer[9], Mario Morvan[4], William Pluriel[13], Mathilde Poveda[14,15], Nour Skaf[4,9,16], Niall Whiteford[17,18], Sam Wright[4], Kai Hou Yip[4], Tiziano Zingales[13], Benjamin Charnay[9], Pierre Drossart[9,10], Jérémy Leconte[13], Olivia Venot[14], Ingo Waldmann[4], and Jean-Philippe Beaulieu[10,19]

[1] La Sapienza Universitá di Roma, Department of Physics, Piazzale Aldo Moro 2, I-00185 Roma, Italy; lorenzo.mugnai@uniroma1.it
[2] INAF—Osservatorio Astronomico di Palermo, Piazza del Parlamento 1, I-90134 Palermo, Italy
[3] University of Palermo, Department of Physics and Chemistry, Via Archirafi I-36, Palermo, Italy
[4] Department of Physics and Astronomy, University College London, London, UK
[5] Max-Planck-Institut für Astronomie, Königstuhl 17, D-69117 Heidelberg, Germany
[6] Instituto de Astrofísica de Canarias (IAC), E-38205 La Laguna, Tenerife, Spain
[7] Institute of Astronomy, KU Leuven, Celestijnenlaan 200D, B-3001 Leuven, Belgium
[8] College of Engineering, Mathematics and Physical Sciences, Physics Building, University of Exeter, Exeter, UK
[9] LESIA, Observatoire de Paris, Université PSL, CNRS, Sorbonne Université, Université de Paris, Meudon, France
[10] Sorbonne Universités, UPMC Université Paris 6 et CNRS, UMR 7095, Institut d'Astrophysique de Paris, Paris, France
[11] Dipartimento di Fisica, Universitá degli Studi di Torino, via Pietro Giuria 1, I-10125 Torino, Italy
[12] INAF Osservatorio Astrofisico di Torino, Via Osservatorio 20, I-10025 Pino Torinese, Italy
[13] Laboratoire d'astrophysique de Bordeaux, Univ. Bordeaux, CNRS, B18N, allée Geoffroy Saint-Hilaire, F-33615 Pessac, France
[14] Laboratoire Interuniversitaire des Systèmes Atmosphériques (LISA), UMR CNRS 7583, Université Paris-Est-Créteil, Université de Paris, Institut Pierre Simon Laplace, Créteil, France
[15] Maison de la Simulation, CEA, CNRS, Univ. Paris-Sud, UVSQ, Université Paris-Saclay, F-91191 Gif-sur-Yvette, France
[16] Subaru Telescope, National Astronomical Observatory of Japan, 650 North A'ohoku Place, Hilo, HI 96720, USA
[17] Institute for Astronomy, University of Edinburgh, Royal Observatory, Blackford Hill, Edinburgh, EH9 3HJ, UK
[18] Centre for Exoplanet Science, University of Edinburgh, UK
[19] School of Physical Sciences, University of Tasmania, Private Bag 37 Hobart, Tasmania 7001, Australia
Received 2020 December 1; revised 2021 March 26; accepted 2021 March 29; published 2021 May 26

Abstract

We present a study on the spatially scanned spectroscopic observations of the transit of GJ 1132 b, a warm ($\sim$500 K) super-Earth (1.13 $R_{\oplus}$) that was obtained with the G141 grism (1.125–1.650 μm) of the Wide Field Camera 3 (WFC3) on board the Hubble Space Telescope. We used the publicly available Iraclis pipeline to extract the planetary transmission spectra from the five visits and produced a precise transmission spectrum. We analyzed the spectrum using the TauREx3 atmospheric retrieval code, with which we show that the measurements do not contain molecular signatures in the investigated wavelength range and are best fit with a flat-line model. Our results suggest that the planet does not have a clear primordial, hydrogen-dominated atmosphere. Instead, GJ 1132 b could have a cloudy hydrogen-dominated atmosphere, have a very enriched secondary atmosphere, be airless, or have a tenuous atmosphere that has not been detected. Due to the narrow wavelength coverage of WFC3, these scenarios cannot be distinguished yet, but the James Webb Space Telescope may be capable of detecting atmospheric features, although several observations may be required to provide useful constraints.

Unified Astronomy Thesaurus concepts: Exoplanet atmospheres (487); Astronomy data analysis (1858); Hubble Space Telescope (761); Exoplanets (498)

1. Introduction

One major obstacle that exoplanetary researchers encounter is a general lack of data. This makes it difficult to determine the composition and internal structure of exoplanets, as there is an inevitable strong degeneracy when one tries to fit a model to observations. By making use of geophysical and statistical principles, several studies have determined the degree of degeneracy in exoplanet compositions (e.g., Adams et al. 2008; Valencia et al. 2013; Dorn et al. 2017). They found that knowing the mass and radius of a planet precisely can lead to superior constraints on the ice mass fraction and size of the inner embryo but little improvement on the atmospheric composition. However, they also found that determining the atmospheric composition (such as from spectroscopy) could lead to a significant improvement of the interior predictions. Therefore, there is a strong motivation to characterize exoplanetary atmospheres, as this would lead to a better understanding on the global properties of their host planets.

In spite of this, under most circumstances only the mass and radius of exoplanets are known, so all that can be done is constrain the internal compositions from the bulk mean densities (e.g., Zeng & Sasselov 2013; Zeng et al. 2016). Recent advances in exoplanetary spectroscopy have allowed for the atmospheric composition and structure to be constrained enough to attain a more holistic understanding of the planet. For instance, from the mass and radius of a planet one cannot tell whether a super-Earth or sub-Neptune is H_2O-rich or a

* Ariel Retrieval Exoplanet School.

silicate embryo with a hydrogen envelope (e.g., Valencia et al. 2013). However, if one were to constrain the atmospheric composition of these perplexing bodies, then one could determine whether the planet is icy (i.e., no atmosphere or an H_2O-rich one if the temperature is high enough) or rocky with a hydrogen-rich atmosphere (i.e., collisional absorption lines of hydrogen are detected with, perhaps, some mineral or volcanic species).

A number of studies using the Wide Field Camera 3 (WFC3) on board Hubble Space Telescope (HST) have found evidence for molecular absorption in sub-Neptunes (e.g., Guo et al. 2020; Guilluy et al. 2021). Of particular note are the studies of the habitable-zone planet K2-18 b, which likely has a hydrogen-helium envelope with a high concentration of water vapor (Benneke et al. 2019; Tsiaras et al. 2019) and possibly CH_4 (Bézard et al. 2020; Blain et al. 2021). Meanwhile, GJ 1214 b most probably hosts a thick cloud layer, with molecular features belonging to a cloud-free primary atmosphere, or one composed of 100% H_2O and 100% CO_2, having been ruled out (e.g., Kreidberg et al. 2014).

While the atmospheric spectroscopy of small, potentially rocky exoplanets is difficult, several analyses have already been made on well-known systems. For example:

1. TRAPPIST-1 b, c, d, e, f, and g most probably do not have cloud-free hydrogen atmospheres (e.g., de Wit et al. 2016).
2. The HST WFC3 transmission spectrum of the highly irradiated super-Earth 55 Cnc e shows evidence for hydrogen cyanide (HCN; Tsiaras et al. 2016a). However, the exact nature of its atmosphere, and whether it exists, is still highly debated (Madhusudhan et al. 2012; Dorn et al. 2019; Jindal et al. 2020; Modirrousta-Galian et al. 2020a; Zhang et al. 2021; Zilinskas et al. 2021).
3. LHS 1140 b, a super-Earth orbiting in the habitable zone of its star, potentially hosts an atmosphere containing water vapor, but the low signal-to-noise ratio and narrow wavelength coverage of the data mean that this detection is tentative (Edwards et al. 2021).

Additionally, the Spitzer phase curve of the terrestrial planet LHS 3844 b is incompatible with a thick atmosphere (Kreidberg et al. 2019). Thus, so far, there have been no definitive measurements of the atmosphere of a rocky exoplanet.

In this paper we perform a spectroscopic analysis of GJ 1132b with the aim of determining its atmospheric composition. Making use of the mass and radius measurements from the literature, we then make inferences on the interior composition and properties of GJ 1132b. Having a mass, radius, and equilibrium temperature of $1.66 \pm 0.23\, M_{\oplus}$, $1.130 \pm 0.056\, R_{\oplus}$, and 500–600 K (Bonfils et al. 2018), respectively, GJ 1132b is a super-Earth that may be an ice planet that migrated inward, or a silicate embryo with a hydrogen envelope (see Figure 1). A mixture of these two compositions or a more exotic makeup may also be possible (Zeng et al. 2016).

In order to try to overcome this degeneracy, we perform a spectroscopic analysis on the spectral data obtained through HST observations. Using five transit observations, we recover a flat spectrum that shows no sign of atmospheric features. We rule out a clear hydrogen/helium-dominated atmosphere to $>5\sigma$. Future observations are required to confidently distinguish between a cloudy primary atmosphere and one with a higher mean molecular weight.

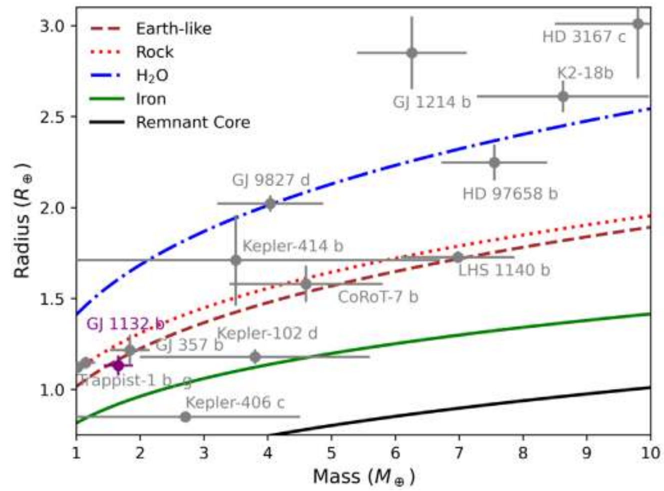

Figure 1. Mass and radius plot of GJ 1132 b (Bonfils et al. 2018) with other super-Earths and sub-Neptunes. The Earth-like, H_2O and iron mass and radius models are from Zeng & Sasselov (2013) and Zeng et al. (2016). The remnant core model (i.e., a planet that is highly compressed as a result of once hosting a large primordial atmosphere that was then subsequently lost) is from Mocquet et al. (2014). It is important to note that the mass–radius models shown above are merely illustrative, as more complex setups are possible (e.g., Jespersen & Stevenson 2020; Modirrousta-Galian et al. 2020a; Mousis et al. 2020). The planets listed are Trappist-1 b, g (de Wit et al. 2016; Grimm et al. 2018), GJ 357 b (Luque et al. 2019), Kepler-406 c (Marcy et al. 2014), Kepler-414 b (Hadden & Lithwick 2014), Kepler-102 d (Marcy et al. 2014), GJ 9827 d (Rice et al. 2019), GJ 1214 b (Harpsøe et al. 2013), CoRoT-7 b (Dai et al. 2019), HD 97658 b (Van Grootel et al. 2014; Guo et al. 2020), HD 3167 c (Christiansen et al. 2017; Guilluy et al. 2021; Mikal-Evans et al. 2021), LHS 1140 b (Ment et al. 2019), and K2-18b (Benneke et al. 2019; Tsiaras et al. 2019; Bézard et al. 2020; Blain et al. 2021).

Table 1
Star and Planet Parameters Used as a Reference in This Paper

Parameter	Value	Source
	Stellar Parameters	
Spectral type	M4.5 V	Berta-Thompson et al. (2015)
$T_{\rm eff}$ (K)	3270 ± 140	Bonfils et al. (2018)
$R_\star$ ($R_\odot$)	$0.2105^{+0.0102}_{-0.0085}$	Bonfils et al. (2018)
$\log_{10} g$ (cm s^{-2})	5.05 ± 0.074	Bonfils et al. (2018)
[Fe/H]	-0.12 ± 0.15	Berta-Thompson et al. (2015)
	Planetary Parameters	
M_p ($M_\oplus$)	1.66 ± 0.23	Bonfils et al. (2018)
R_p ($R_\oplus$)	1.130 ± 0.056	Bonfils et al. (2018)
P (days)	1.628931 ± 0.000027	Bonfils et al. (2018)
$a/R_\star$	$15.6235^{+0.8}_{-0.7}$	Bonfils et al. (2018)[a]
e	< 0.22[b]	Bonfils et al. (2018)
i (deg)	$88.68^{+0.40}_{-0.33}$	Bonfils et al. (2018)
$T_{\rm mid}$ (BJD −2,450,000)	7184.55786 ± 0.00031	Bonfils et al. (2018)

Notes.
[a] Derived from Bonfils et al. (2018) measurements of a and $R_\star$.
[b] Fixed to zero as in Berta-Thompson et al. (2015).

2. Method

2.1. Data Analysis

Our analysis is based on five transit observations of GJ 1132b (Table 1) obtained between 2017 April and November with the G141 infrared grism (1.125–1.650 μm) of the WFC3 on board

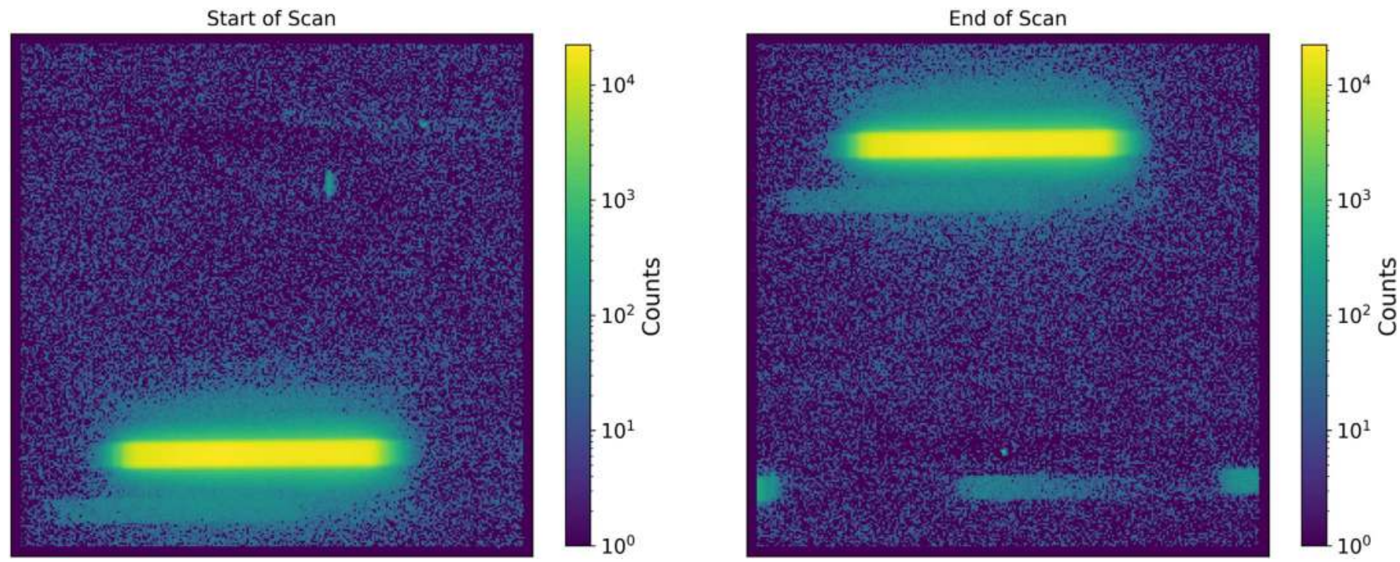

Figure 2. Example reads from the beginning (left) and end (right) of a scan for the second visit. If the data were not extracted from each read individually, the two faint background sources would contribute to the spectrum. The color indicates the count per pixel and is represented with a log scale.

HST. The observations were part of the HST proposal No. 14758 led by Zach Berta-Thompson (Berta-Thompson et al. 2016) and were downloaded from the public Mikulski Archive for Space Telescope (MAST) archive.[20]

Each transit observation required four HST orbits and utilized the spatial scanning technique. The observations were acquired using the 256×256 subarray, employing the SPARS10 sampling sequence with 15 up-the-ramp reads that lead to an exposure time of 103.129 s. The scan speed was $0\farcs2$ s^{-1}, leading to a total scan length of 170 pixels and a maximum pixel fluence below 24,000 electrons.

Following the procedure already described in similar studies (e.g., Anisman et al. 2020; Edwards et al. 2020a; Skaf et al. 2020; Changeat & Edwards 2021), we extract white and spectral light curves from the raw HST/WFC3 images using the Iraclis software (Tsiaras et al. 2016c). Iraclis is an open-source software dedicated to the analysis of WFC3 scanning observations and is publicly available on GitHub.[21] In the following we briefly summarize the data analysis steps operated by the software, but we refer the reader to Tsiaras et al. (2016c) for a complete discussion.

2.1.1. Data Reduction and Calibration

The Iraclis reduction process included the following steps: zero-read subtraction, reference pixel correction, nonlinearity correction, dark current subtraction, gain conversion, sky background subtraction, calibration, flat-field correction, and corrections for bad pixels and cosmic rays (Tsiaras et al. 2016c). In each of the visits, we noted several faint sources that overlapped with the spectrum for GJ 1132. Hence, we split these data into individual up-the-ramp reads and performed the extraction on these to remove the signal from these secondary sources that could impact the shorter wavelengths of the recovered spectrum. Two example reads from the second visit are shown in Figure 2, with the first-order spectrum from the faint source visible below the data from GJ 1132 and the zeroth-order spectrum of another star also within the scan's arc.

2.1.2. Light-curve Extraction

We extract the wavelength-dependent light curves taking into account the geometric distortions caused by the tilted detector of the WFC3/IR channel.

We obtain a *white light curve* and a set of *spectral light curves*. The former is obtained integrating the full wavelength range of WFC3/G141, while the latter are extracted using a narrow band such that the resolving power is 70 at 1.4 μm.

2.1.3. Limb-darkening Coefficients

The limb-darkening coefficients are computed using the nonlinear formula by Claret (2000), which scales the intensity emerging from the star as

$$\frac{I(\mu)}{I(1)} = 1 - \sum\nolimits_{k=1}^{4} a_k (1 - \mu^{\frac{k}{2}}), \tag{1}$$

where $\mu = \cos(\gamma)$, with γ the angle between the line of sight and the emergent intensity, and a_k are the limb-darkening coefficients.

We calculated the a_k coefficients using `ExoTETHyS` (Morello et al. 2020), with the stellar models from Phoenix 2018 (Claret 2018) and the parameters in Table 1. These are given in Table 2.

2.1.4. White Light-curve Fitting

To fit the extracted white and spectral light curves, we consider the known time-dependent systematics introduced by HST:

1. long-term "ramp," characterized by a linear trend;
2. short-term "ramp," characterized by an exponential trend.

To remove these systematics, we multiply by a normalization factor n_w and an instrumental corrective factor $R(t)$. The former depends on the telescope observing scanning mode, n_w^{scan}, and

[20] https://archive.stsci.edu/hst/
[21] https://github.com/ucl-exoplanets/Iraclis

Table 2
Limb Darkening Coefficients Used Here. The First Row Represents the White light Curve while all others are for the Spectral Light Curves

λ [μm]	a1	a2	a3	a4	$\Delta\lambda$ [μm]
1.3840	1.475	−1.351	0.830	0.592	
1.1262	1.461	−1.439	0.922	−0.247	0.0219
1.1478	1.435	−1.431	0.924	−0.249	0.0211
1.1686	1.413	−1.412	0.912	−0.246	0.0206
1.1888	1.430	−1.443	0.934	−0.252	0.0198
1.2084	1.406	−1.406	0.907	−0.244	0.0193
1.2275	1.363	−1.363	0.880	−0.237	0.0190
1.2465	1.364	−1.361	0.876	−0.236	0.0189
1.2655	1.361	−1.371	0.886	−0.239	0.0192
1.2848	1.324	−1.330	0.859	−0.232	0.0193
1.3038	1.318	−1.333	0.862	−0.233	0.0188
1.3226	1.361	−1.386	0.896	−0.241	0.0188
1.3415	1.376	−1.247	0.759	−0.198	0.0189
1.3605	1.447	−1.314	0.787	−0.202	0.0192
1.3800	1.526	−1.468	0.904	−0.236	0.0199
1.4000	1.477	−1.337	0.799	−0.205	0.0200
1.4202	1.456	−1.275	0.746	−0.190	0.0203
1.4406	1.475	−1.288	0.745	−0.187	0.0206
1.4615	1.417	−1.183	0.672	−0.168	0.0212
1.4831	1.461	−1.273	0.735	−0.184	0.0220
1.5053	1.475	−1.316	0.766	−0.193	0.0224
1.5280	1.475	−1.332	0.784	−0.199	0.0230
1.5515	1.452	−1.309	0.772	−0.197	0.0241
1.5762	1.478	−1.374	0.816	−0.208	0.0253
1.6021	1.485	−1.435	0.872	−0.225	0.0264
1.6295	1.475	−1.476	0.917	−0.240	0.0283

Note. The first row represents the white light curve, while all others are for the spectral light curves.

changes to $n_w^{\rm for}$ when scanning direction is upward and to $n_w^{\rm rev}$ when scanning direction is downward. $R(t)$ is time dependent and can be derived as

$$R(t) = (1 - r_a(t - T_0))(1 - r_{b_1}e^{-r_{b_2}(t-t_0)}), \tag{2}$$

where t is time, T_0 is the midtransit time, t_0 is the starting time of each HST orbit, r_a is the linear systematic trend's slope, and r_{b_1} and r_{b_2} are the exponential systematic trend's coefficients (Kreidberg et al. 2014; Tsiaras et al. 2016a, 2016c).

To extract the white transit light curve, $F_w^v(t)$, for each visit, v, we fit the transit model multiplied by the instrumental systematics, $n_w^{\rm scan}R(t)F_w^v(t)$, and we fit the systematic model $R(t)$ on the out-of-transit data, correcting the light curve and then fitting again $n_w^{\rm scan}F_w^v(t)$.

To fit the light curves, we use the data presented in Table 1, leaving as free parameters the radii ratio, $R_p/R_\star$, and the midtransit time, $T_{\rm mid}$. For the fit we used a Markov Chain Monte Carlo of 350,000 steps with 200 walkers and 200,000 burned iterations, using the emcee Python package (Foreman-Mackey et al. 2013). Each light curve has been fitted individually, and so we obtained the white light-curve squared radii ratio for each transit $(R_p/R_\star)^2_{w,v}$. Initially, we fitted the white light curves using the formulae above and the uncertainties per pixel, as propagated through the data reduction process. However, it is common in HST/WFC3 data to have additional scatter that cannot be explained by the ramp model. For this reason, we scaled up the uncertainties in the individual data points, for their median to match the standard deviation of the residuals, and repeated the fitting (Tsiaras et al. 2018). The resulting detrended white light curves are reported in Figure 3, and the fit results are in Table 3. The table shows that the $(R_p/R_\star)^2_{w,v}$ are compatible under 2σ and that the standard deviations of the fitting residuals for the white light curves are significantly higher than the photon noise. The ratio between the standard deviation of the fitting residuals and the photon noise is reported in Table 3 as $\bar{\sigma}$.

2.1.5. Spectral Light-curve Fitting

To correct for the systematics present in the spectral light curves of each visit, $F_\lambda^v(t)$, we fit each curve with a model that includes the associated white light curve, $F_w^v(t)$:

$$n_\lambda^{\rm scan}[1 - r_a(t - T_0)]\frac{F_\lambda^v(t)}{F_w^v(t)}, \tag{3}$$

where r_a is the coefficient of a wavelength-dependent linear slope along each HST visit and $n_\lambda^{\rm scan}$ is the normalization factor, which changes to $n_\lambda^{\rm for}$ when the scanning direction is upward and to $n_\lambda^{\rm rev}$ when it is downward. In the spectral light-curve fitting, the only free parameter is $R_{\rm p}/R_\star$, while the other parameters are the same as we used for the white light-curve fitting. For the fit we used a Markov Chain Monte Carlo of 150,000 steps with 100 walkers and 100,000 burned iterations, using again the emcee package (Foreman-Mackey et al. 2013).

To check the quality of our fits, we use the autocorrelation of the residuals for each light curve using the numpy correlate package. To determine a "good" value of the autocorrelation, we generated 1000 instances of random Gaussian noise and computed the autocorrelation. For the number of data points in our light curves (∼70), 85% of the time the autocorrelation of Gaussian noise is below 0.35. For each of our spectra, the autocorrelation is smaller than 0.32 (see Table 3), and thus any correlations found are consistent with those found in Gaussian noise.

We also check the success of our fit by computing the reduced chi-squared from the comparison between the data and the model ($\bar{\chi}$), as well as the standard deviation of the residuals with respect to the photon noise ($\bar{\sigma}$). The reduced chi-squared between the spectral light curves for each visit is between 1.16 (second visit) and 1.2 (fourth visit). The averaged standard deviation of the residuals with respect to the formal photon noise is between 1.03 (second visit) and 2.42 (fourth visit), and therefore the resulting post-processing total noise is between 6% and 142% greater than the photon noise.

Then, to compare light curves obtained from different visits, $F_\lambda^v(t)$, we correct for offsets by subtracting each spectrum by the corresponding white light-curve depth, $(R_p/R_\star)^2_{w,v}$, and adding the weighted average transit depth of all white light curves, $(R_p/R_\star)^2_w$. Finally, we compute the weighted average from all the transit observations, $(R_p/R_\star)^2_\lambda$, reported in Table 4. The spectral light-curve fits are shown in Figure 4, while the spectrum obtained from each visit and the final average spectrum are shown in Figure 5.

We notice that in each spectral bin the measurements in each observation are generally compatible within 1σ of the mean, as shown in Figure 5. Where data points are not within 1σ, there are no obvious trends with the observation number or wavelength. To assess whether the five transmission spectra obtained are statistically consistent, we perform a Kolmogorov–Smirnov test. We perform this test by comparing the transmission spectra two at a time, in every possible combination, to test the null hypothesis that they come from

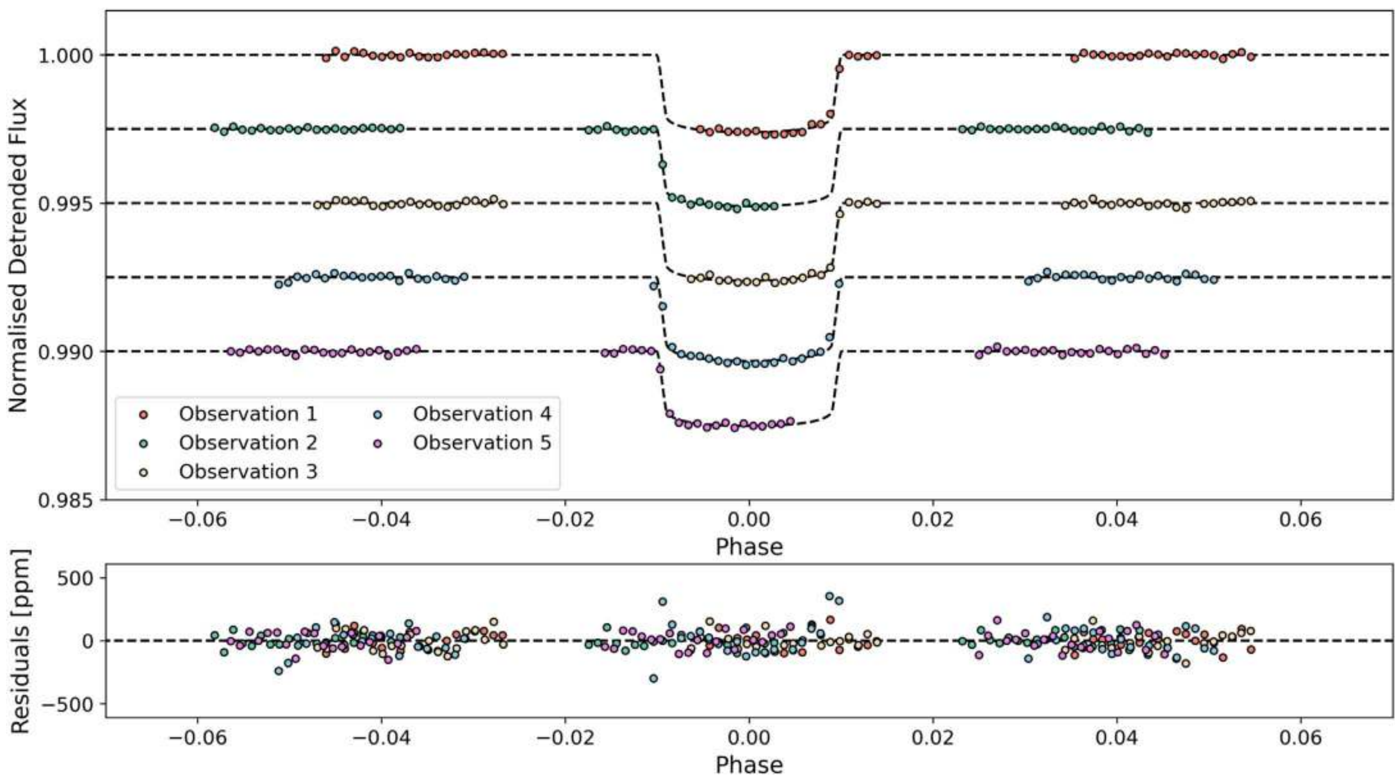

Figure 3. Top panel: detrended white light curves from each visit, along with the best-fit transit model. Bottom panel: residuals.

the same distribution. We use the SciPy package (Virtanen et al. 2020) for the computation. We conclude that we cannot reject the null hypothesis for any of the couples because the minimum resulting p-value is 28%.

2.2. Atmospheric Characterization

To characterize the planetary atmosphere, we use the retrieval code TauREx3[22] (Al-Refaie et al. 2019), the new version of TauREx (Waldmann et al. 2015a, 2015b). The code maps the atmospheric forward model parameter space to find the best fit to the observed spectra. TauREx allows us to identify absorbers in the spectrum using line lists from ExoMol (Tennyson et al. 2016), HITEMP (Rothman et al. 2010), and HITRAN (Rothman et al. 1987). To perform the retrieval, we use the Multinest algorithm (Feroz et al. 2011; Buchner et al. 2014) to sample the parameter space through 1500 live points, and we set the algorithm evidence tolerance to 0.5.

2.2.1. Temperature–Pressure Profile

We simulate the planetary atmosphere assuming an isothermal temperature–pressure profile with constant molecular abundances as a function of altitude. This assumption is driven by the narrow wavelength range investigated in the data, which results in a restricted probed range of the planetary temperature–pressure profile (Rocchetto et al. 2016). We calculated the equilibrium temperatures as

$$T_{\rm eq} = T_\star \left(\frac{R_\star}{2\,a}\right)^{1/2} (1 - A)^{1/4}, \tag{4}$$

where $R_\star$ is the stellar radius, a is the semimajor axis, and A is the Bond albedo. To keep in line with other studies, we adopt a standard Bond albedo of $A = 0.3$ (Bonfils et al. 2018), although we are aware that the albedo is highly sensitive to the planetary properties and could therefore vary significantly (e.g., Marley et al. 1999; Modirrousta-Galian et al. 2021). For the equilibrium temperature we use $T_{\rm eq} = 520 \pm 44$ K, where the uncertainty comes from the error propagation on the stellar parameters and the planet's semimajor axis from Table 1. Then, for the atmospheric retrievals we use a wide range of temperature priors from 0.5 $T_{\rm eq}$ to 1.5 $T_{\rm eq}$ (i.e., 260–780 K).

2.2.2. Atmosphere Composition

For the atmosphere we use the plane-parallel approximation, building 100 plane-parallel layers to uniformly sample in log-space the pressure range from 10^{-4} to 10^{6} Pa. We assume a primary atmosphere of He and H_2 with a fixed ratio between the two molecules of 0.17, and then we introduce the trace gases: H_2O (Barton et al. 2017; Polyansky et al. 2018), CH_4 (Hill et al. 2013; Yurchenko & Tennyson 2014), CO (Li et al. 2015), CO_2 (Rothman et al. 2010), HCN (Barber et al. 2014), and NH_3 (Yurchenko et al. 2011). To perform the atmospheric fit, we use as boundaries for each molecule 10^{-12} and 1 in volume mixing ratios (log-uniform prior). To fit the planet atmosphere, we used two models: one with all the molecules listed above molecules, and a second that also included N_2 (Western et al. 2018). In fact, N_2 is a largely inactive gas over the spectral range considered, and its only contribution is to the atmospheric mean molecular weight. Using such a distinction between the two models, we are considering a light, primary atmosphere while also exploring the potential for a heavy, secondary atmosphere. We note that, as the abundance of all

[22] https://github.com/ucl-exoplanets/TauREx_public

Table 3
Derived Parameters from the White Light Curves and Fitting Metrics: The Reduced Chi-squared ($\bar{\chi}^2$), the Standard Deviation of the Residuals with Respect to the Photon Noise ($\bar{\sigma}$), and the Autocorrelation (AC)

Parameter	First Visit	Second Visit	Third Visit	Fourth Visit	Fifth Visit
$(R_p/R_\star)^2_{w,v}$	$0.002430^{+0.000039}_{-0.000030}$	$0.002430^{+0.000024}_{-0.000017}$	$0.002440^{+0.000040}_{-0.000030}$	$0.002632^{+0.000011}_{-0.000017}$	$0.002352^{+0.000029}_{-0.000029}$
$T_{\rm mid}$ (BJD −2,450,000)	$7862.19152^{+0.00008}_{-0.00009}$	$8020.19899^{+0.00004}_{-0.00004}$	$8077.21035^{+0.00008}_{-0.00007}$	$8080.46887^{+0.00007}_{-0.00007}$	$8083.72719^{+0.00008}_{-0.00005}$
$\bar{\chi}$	1.18	1.16	1.17	1.20	1.17
$\bar{\sigma}$	1.43	1.03	1.50	2.42	1.45
AC	0.13	0.32	0.15	0.11	0.22

Table 4
This Table Reports for Every Spectral Bin the Averaged Transmission Spectra Measured with Combined the Spectral Light Curves Obtained with Iraclis, $(R_p/R_\star)^2_\lambda$

λ [μm]	$(R_p/R_\star)^2_\lambda$	Uncertainty	$\Delta\lambda$ [μm]
1.1263	0.002325	0.000034	0.0219
1.1478	0.002402	0.000033	0.0211
1.1686	0.002376	0.000035	0.0206
1.1888	0.002412	0.000030	0.0198
1.2084	0.002453	0.000031	0.0193
1.2275	0.002441	0.000031	0.0190
1.2465	0.002418	0.000030	0.0189
1.2655	0.002428	0.000031	0.0192
1.2848	0.002425	0.000028	0.0193
1.3038	0.002481	0.000028	0.0188
1.3226	0.002478	0.000028	0.0188
1.3415	0.002428	0.000030	0.0189
1.3605	0.002408	0.000028	0.0192
1.3801	0.002444	0.000029	0.0199
1.4000	0.002439	0.000030	0.0200
1.4202	0.002398	0.000031	0.0203
1.4406	0.002388	0.000029	0.0206
1.4615	0.002377	0.000028	0.0212
1.4831	0.002457	0.000029	0.0220
1.5053	0.002404	0.000029	0.0224
1.5280	0.002438	0.000029	0.0230
1.5516	0.002435	0.000030	0.0241
1.5763	0.002388	0.000027	0.0253
1.6021	0.002416	0.000027	0.0264
1.6295	0.002418	0.000028	0.0283

molecules was allowed to extend to 1 (i.e., 100%), the retrieval without N_2 is also capable of resulting in a high mean molecular weight atmosphere.

Additionally, we include in all our models Rayleigh scattering and collision-induced absorption of H_2–H_2 (Abel et al. 2011; Fletcher et al. 2018) and H_2–He (Abel et al. 2012). Clouds are modeled assuming a gray opacity model, and cloud top pressure bounds are set between 10^{-2} and 10^6 Pa. We also set a large range of priors for the planetary radius, from 0.5 R_p to 1.4 R_p, referring to the literature value reported in Table 1. The planetary radius is assumed to be equivalent at 10^6 Pa pressure.

To assign a significance to our detection, we use the Bayes factor between the nominal atmospheric model and a model that contains no active trace gases, Rayleigh scattering, or collision-induced absorption. We perform a retrieval where no molecular absorbers are active, which provides a flat-line model to test the significance of retrievals including molecular opacities.

3. Results

The final spectrum recovered is extremely flat, with few deviations from a flat line. Nevertheless, we conducted retrievals

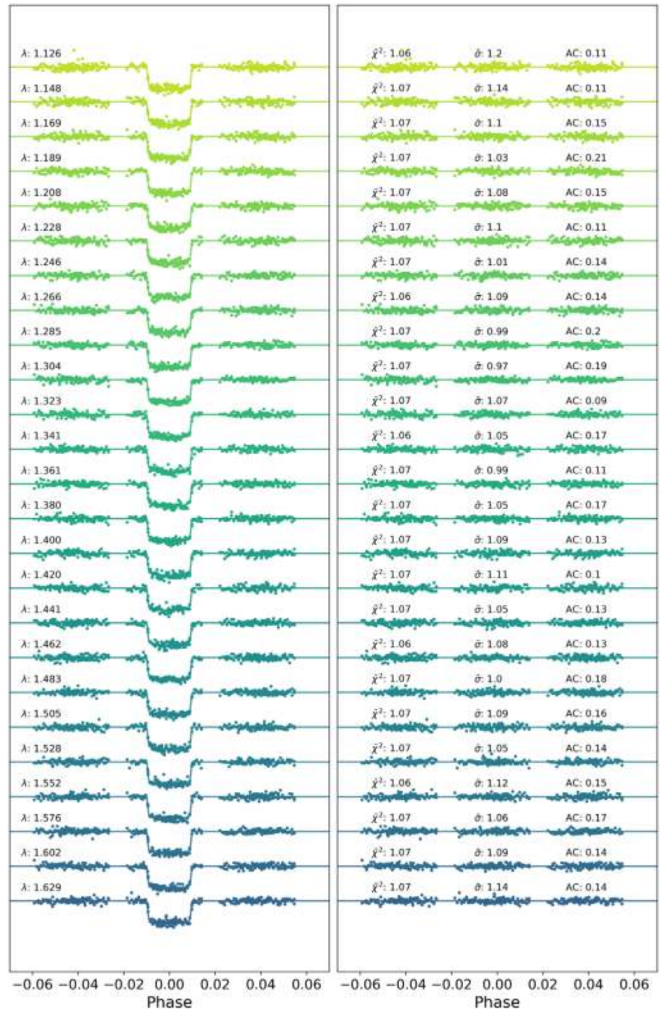

Figure 4. Spectral light curves fitted with Iraclis for the transmission spectra where, for clarity, an offset has been applied. Left: detrended spectral light curves with best-fit model plotted. Right: residuals from the fitting with mean values for the reduced chi-squared ($\bar{\chi}^2$), the standard deviation of the residuals with respect to the photon noise ($\bar{\sigma}$), and the autocorrelation (AC) across the five transits.

to explore the possibility that any of these minor features could be attributed to molecular species. While formation and evolution theories suggest that a hydrogen-dominated atmosphere is unlikely for this planet, we started by exploring this possibility. Our initial retrieval, conducted with a hydrogen-dominated atmosphere containing clouds and the molecules discussed in Section 2.2, found no evidence of features. The retrieval including N_2 came to similar results, with the spectrum essentially being fitted by a gray cloud deck alone in both cases. The Bayesian evidence for each retrieval, $\log(E) = 215.97$ and

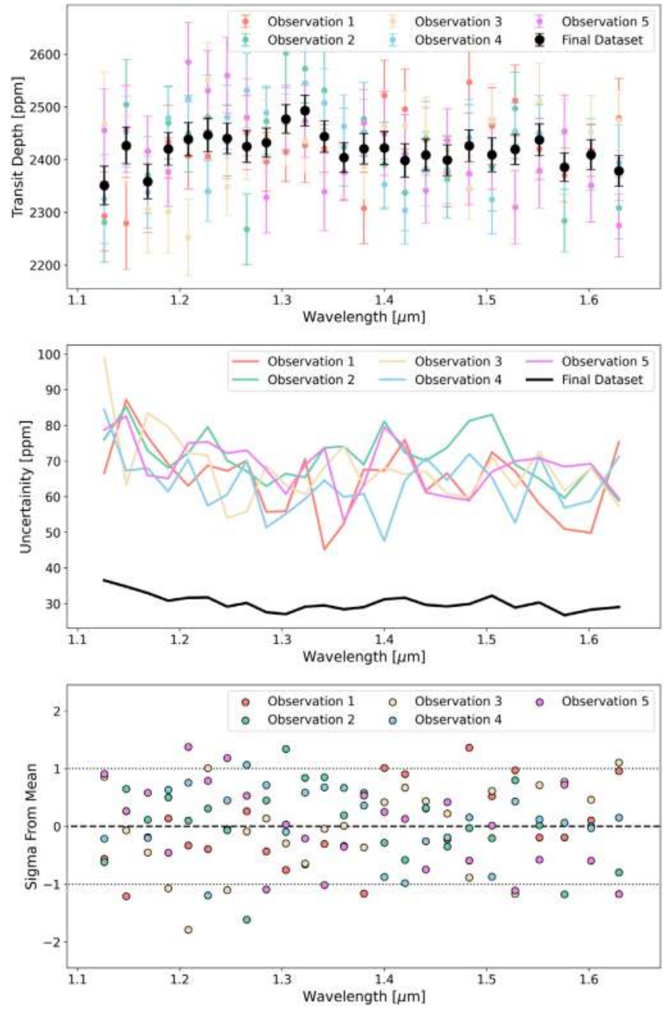

Figure 5. Top panel: transmission spectral data collected in each visit with their uncertainties (colored data points) and the average transmission spectrum (black) obtained from their combination. Middle panel: uncertainty of each data point. Bottom panel: divergence from the mean, in sigma, of each data point.

$\log(E) = 216.12$ for retrievals with and without N_2, respectively, shows that the cloud-only model ($\log(E) = 218.52$) provides the best fit to the data.

To better show the noncompliance of our data with molecular features, we performed retrievals for clear hydrogen-dominated atmospheres with only one molecule that was forced to mixing ratios from 10^{-6} to 10^{-1}. The latter is set as a rough boundary between primary and secondary atmospheres (i.e., a mean molecular weight $\gg 2.3$). We use the Bayesian evidence from these retrievals, given in Figure 6, to rule them out to a given significance. We ran these for H_2O, NH_3, CO, CO_2, CH_4, and HCN, and in every case the cloud-only model provided a better fit to the data to $>5\sigma$. Hence, our results suggest that we can rule out a clear, primary atmosphere with high confidence: if GJ 1132b hosts a primary atmosphere (i.e., one dominated by hydrogen and helium), according to our spectrum, the planet must be completely overcast.

We also attempted to fit several models with secondary atmospheric compositions. These were atmospheres composed entirely of H_2O and CO_2 (i.e., $\mathrm{VMR}_{H_2O} = 1$ and $\mathrm{VMR}_{CO_2} = 1$), as well as an atmosphere similar to that of Venus (with volume mixing ratios of $\mathrm{VMR}_{CO_2} = 0.965$, $\mathrm{VMR}_{H_2O} = 2\mathrm{e}{-5}$, $\mathrm{VMR}_{CO} = 1.7\mathrm{e}{-5}$, $\mathrm{VMR}_{SO_2} = 1.5\mathrm{e}{-4}$). For each of these, a cloud-free atmosphere was assumed and the molecular abundances were again fixed. Thus, the only free parameters were the planet radius and the temperature. The best-fit spectrum in each case is given in Figure 7, although with the Bayesian evidence for each setup. Again, the best-fitting model is that of a flat line, with a cloud-free, 100% H_2O atmosphere being ruled out to $>3\sigma$. However, while providing worse fits to the data than the cloud-only model, the clear, 100% CO_2 and Venusian atmosphere models cannot be definitively ruled out with the current data set.

Hence, no evidence for molecular features could be extracted from this data set. For completeness we include the posterior distribution for our baseline retrieval in Figure 8. Our results suggest that the atmosphere of GJ 1132b is likely to be cloudy but that certain enriched atmospheres, with small scale heights that led to only minor features over the HST WFC3 range, could also explain the data. A final possibility, which is compatible with our spectrum, is that the planet hosts an atmosphere too thin to be detected and that we are measuring the transit depth caused by the planet's solid surface.

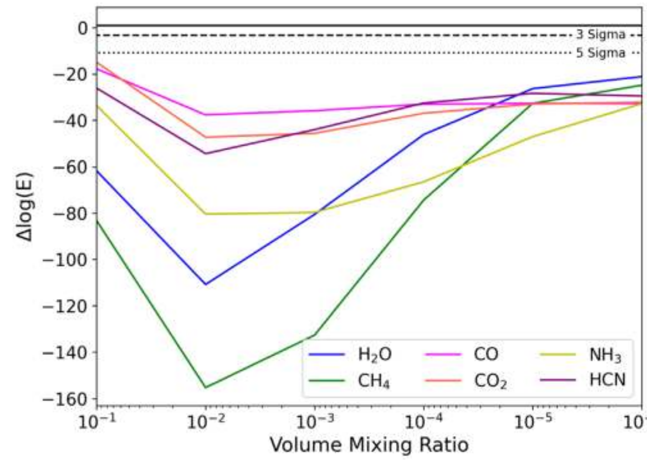

Figure 6. Comparison of the log evidence for a cloudy atmosphere to that of single molecule retrievals where the abundance of said molecule was fixed and no clouds were included. In each case, the cloudy model is preferred to $>5\sigma$.

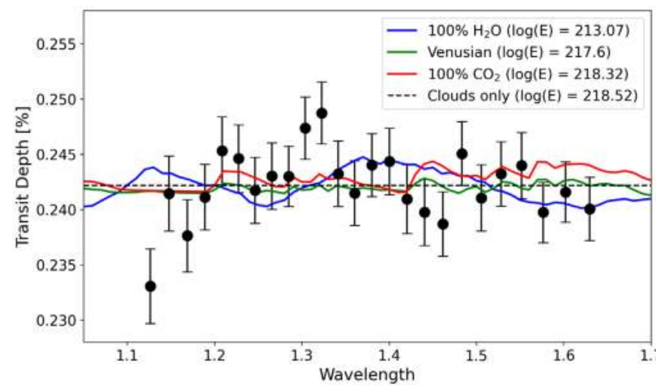

Figure 7. Best-fit spectra for the secondary atmosphere models. The cloud-only model (i.e., a flat line) still provides the best fit to the spectrum obtained.

4. Discussion

4.1. Statistical Goodness-of-fit Analysis

Due to the absence of molecular features in the measured spectrum, we statistically compare the data reported in Table 4

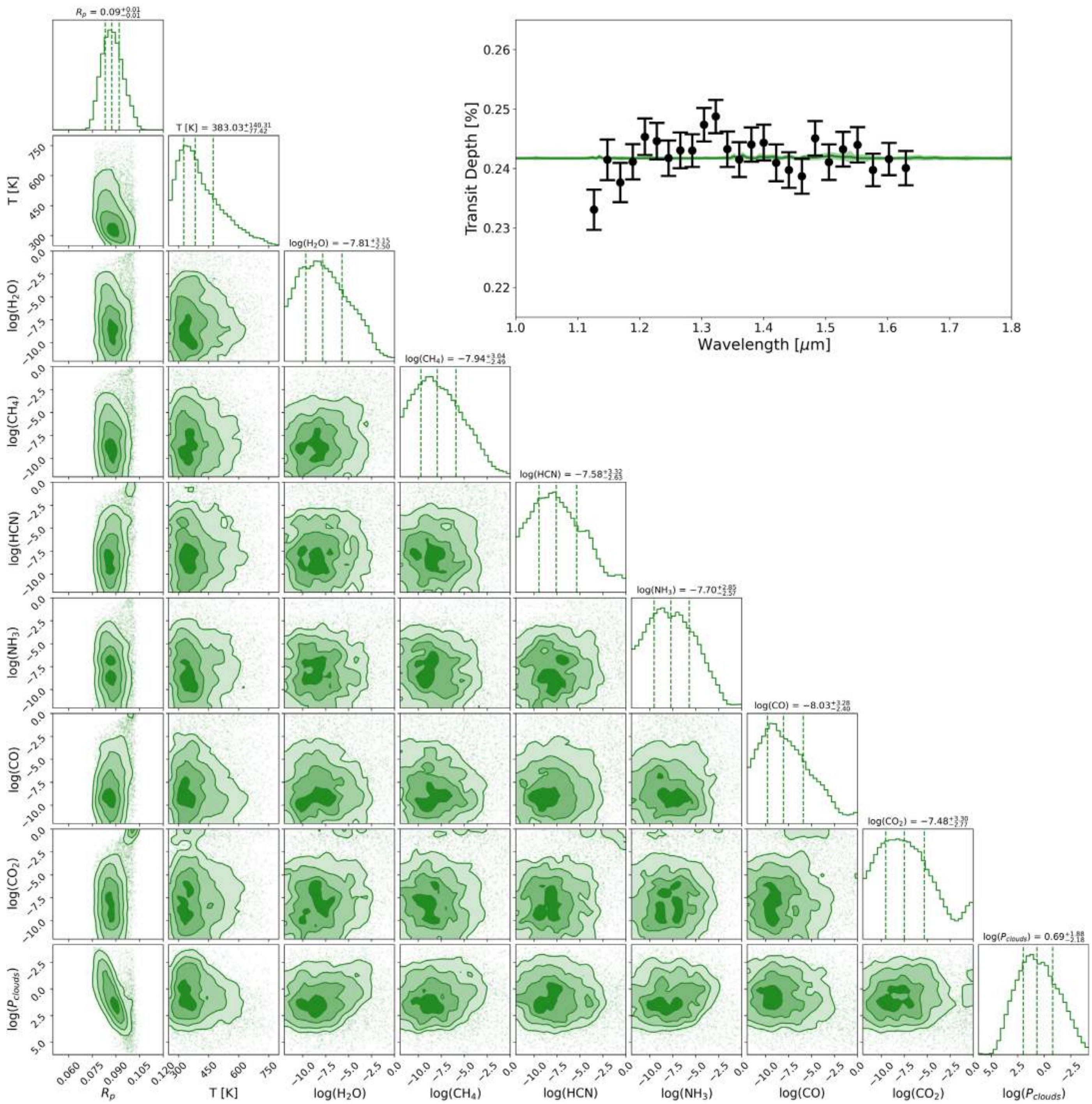

Figure 8. Inset top right: transmission spectra extracted with Iraclis software from the five HST visits of GJ 1132b. In black is reported the average transmission spectra, while the green line is the spectrum retrieved with TauREx, and the shaded region represents the 3σ confidence level. Left: retrieval posteriors for GJ 1132b, which show no evidence for molecular species.

with a constant value defined as the weighted average of the planetary-to-stellar radius ratios. By using chi-squared statistics, we obtain $\chi^2 = 26$ with $\nu = 25 - 1 = 24$ degrees of freedom. The obtained reduced chi-squared value is $\chi^2_\nu = 26/24 = 1.08$, with an uncertainty of $\sigma_{\chi^2_\nu} = 0.29$. Because $\chi^2_\nu \sim 1$, we cannot exclude the possibility that the measured data come from a constant distribution, as the flat line is a good model to describe the data. Therefore, the collected data do indeed show no detectable molecular features.

Because we compare different observations to obtain the spectrum in Table 4, we perform a jack-knife analysis (Quenouille 1949, 1956; Tukey 1958). This consists of taking the original data set, X, which is composed of n samples, and creating n new data sets, x_i. Each new data set is like the original except that it has $n - 1$ samples. The removed sample is different for each new data set so that no two are identical. In our case we have five observations, so $n = 5$. For each of these new samples we compute the average spectrum, as described in Section 2.1.5, and then we compare it with its weighted average

Table 5
Reduced Chi-squared (χ^2_ν) from Jackknife Analysis

Rem. Obs.	χ^2_ν
1	1.3
2	0.6
3	1.6
4	1.0
5	1.2

Note. The first column reports the observation that has been removed from the data set before computing the chi-squared. The second column reports the resulting reduced chi-squared of the comparison between the data set average spectrum and its weighted average value, for the data set without the removed observation.

value, $\hat{x}_i$. In the same manner as before, we make use of the reduced chi-squared value χ^2_ν as a metric for the goodness of the fit. The results are reported in Table 5. All of our χ^2_ν are $\sim$1, indicating a very good fit. This confirms our results and demonstrates that we are not biased in our analysis.

We also computed the jackknife bias as $bias = (n - 1)(\hat{X} - \hat{x}) = 3e - 7$, where $\hat{X}$ is the average radii ratio computed from the X sample and $\hat{x}$ is the average of the mean radii ratios $\hat{x}_i$. The measured bias is two orders of magnitude smaller than the uncertainties and can therefore be neglected.

4.2. The Physical Implications of Our Results

As explained previously, from mass and radius measurements it is not always possible to accurately determine the bulk composition of an exoplanet. However, there are a few clues that could help us evaluate whether GJ 1132 b could have a hydrogen atmosphere or not. Specifically, one could consider the effects of X-ray and ultraviolet (XUV) irradiation from the host star and its effects on a primordial atmosphere. Performing a backward reconstruction of the maximum amount of hydrogen that could be lost by XUV irradiation is beyond the scope of this study, but it is worth discussing.

Consider, for example, the super-Earth GJ 357 b. Having a mass, radius, and temperature of $\simeq$1.84 $M_\oplus$, $\simeq$1.22 $R_\oplus$, and $\simeq$500 K (Luque et al. 2019), respectively, its properties are relatively similar to those of GJ 1132 b. However, what makes GJ 357 b unique is that it orbits a very low active M-type star (Modirrousta-Galian et al. 2020b). In spite of the abnormally low XUV levels, a careful backward evaporation reconstruction model shows that up to $\sim$38 $M_\oplus$ of hydrogen could have been lost (Modirrousta-Galian et al. 2020b). Although GJ 357 b was probably born with a hydrogen envelope significantly smaller than this (perhaps $M_{\rm atm} \lesssim 0.02\, M_\oplus$; Ikoma & Hori 2012; Chachan & Stevenson 2018), this calculation shows that even stars with very low activity levels could completely strip off the primordial atmosphere of a planet. While the activity level of GJ 1132 is not known, statistically speaking it is most probably higher than that of GJ 357 b (e.g., Penz & Micela 2008; Sanz-Forcada et al. 2011), so by comparison one can infer that GJ 1132 b most probably lost its hydrogen envelope. Of course, other effects such as magnetism (e.g., Matsakos et al. 2015), magma–atmosphere exchanges (e.g., Chachan & Stevenson 2018), and migration (e.g., Nayakshin & Lodato 2012) may have lowered the evaporation rates, but large mass losses would be expected nonetheless. Therefore, based on the

Table 6
Collection of Transit Depths of GJ 1132b from Other Instruments

Instrument	λ (μm)	$(R_p/R_\star)^2$	Reference
Spitzer	4.50	0.00242 $\pm$ 0.00008	D17
MEarth	2.19	0.00207 $\pm$ 0.00005	D17
LDSS3C	0.71	0.00240 $\pm$ 0.00010	DL18
LDSS3C	0.73	0.00206 $\pm$ 0.00010	DL18
LDSS3C	0.75	0.00219 $\pm$ 0.00009	DL18
LDSS3C	0.77	0.00233 $\pm$ 0.00009	DL18
LDSS3C	0.79	0.00214 $\pm$ 0.00009	DL18
LDSS3C	0.81	0.00234 $\pm$ 0.00009	DL18
LDSS3C	0.83	0.00212 $\pm$ 0.00009	DL18
LDSS3C	0.85	0.00229 $\pm$ 0.00009	DL18
LDSS3C	0.87	0.00229 $\pm$ 0.00009	DL18
LDSS3C	0.89	0.00233 $\pm$ 0.00009	DL18
LDSS3C	0.91	0.00218 $\pm$ 0.00008	DL18
LDSS3C	0.93	0.00222 $\pm$ 0.00009	DL18
LDSS3C	0.95	0.00206 $\pm$ 0.00010	DL18
LDSS3C	0.97	0.00220 $\pm$ 0.00010	DL18
LDSS3C	0.99	0.00210 $\pm$ 0.00010	DL18
LDSS3C	1.01	0.00223 $\pm$ 0.00012	DL18
LDSS3C	1.03	0.00228 $\pm$ 0.00016	DL18
TESS	0.8	0.002312 $\pm$ 0.000093	This work

Note. D17: Dittmann et al. (2017); DL18: Diamond-Lowe et al. (2018). Data from Table 3 of Dittmann et al. (2017) and from Table 6 of Diamond-Lowe et al. (2018).

mass–radius relation of GJ 1132 b, our current understanding of XUV-induced evaporation, and our spectroscopic results, a strong argument can be made that GJ 1132 b is a telluric body lacking a primordial envelope that instead might host a secondary atmosphere. However, we do acknowledge that other setups are plausible. For instance, GJ 1132 b could be an airless rocky planet (e.g., Modirrousta-Galian et al. 2021) or a rocky planet without clouds but an atmosphere that is too thin to be detected in these data. Notwithstanding, these configurations may be less probable given that geological outgassing is expected to generate thick secondary atmospheres with clouds (Kite et al. 2009; Noack et al. 2017; Dorn et al. 2018).

4.3. Comparison with Previous Works

To compare our measurements with previous works, we adopt the radius ratios published in recent papers. We use the measurements from Table 3 of Dittmann et al. (2017) and Table 6 of Diamond-Lowe et al. (2018), and we compute the $(R_p/R_\star)^2$ from them, where needed. Additionally, GJ 1132b has also been studied by TESS, and we used the pipeline from Edwards et al. (2020b) to download, clean, and fit the 2-minute cadence Pre-search Data Conditioning (PDC) light curves (Smith et al. 2012; Stumpe et al. 2012, 2014). Then, we report all the data in Table 6 and in Figure 9.

While it has become common to combine data from different instruments, there may be an offset between the data sets. These offsets can occur owing to imperfect correction of instrument systematics, from the use of different orbital parameters or limb-darkening coefficients during the light-curve fitting, or from stellar variability or activity (e.g., Stevenson et al. 2014a, 2014b; Morello et al. 2017; Tsiaras et al. 2018; Bruno et al. 2020; Yip et al. 2020, 2021; Changeat et al. 2020; Murgas et al. 2020; Pluriel et al. 2020; Schlawin et al. 2021). As there is no wavelength overlap between our HST observations and the

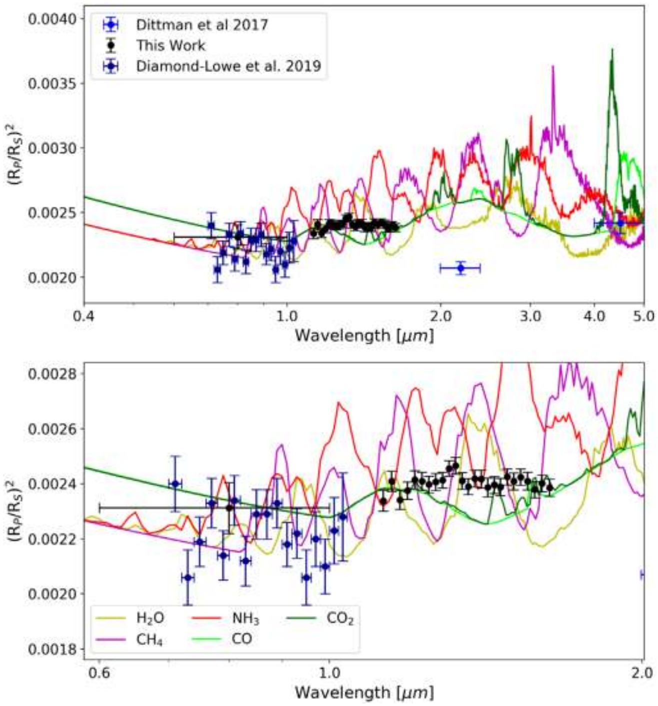

Figure 9. Transit depths from various studies on GJ 1132b, as listed in Table 6, and the spectrum recovered in this work. Also plotted are forward models that assume a clear H/He atmosphere with various molecules, each at an abundance of volume mixing ratios of 10^{-3}. We note that we do not directly compare the models to the combined data set owing to the possibility of incompatibilities between them.

ground-based data, we cannot be certain of the compatibility of the observations.

The transit depth from the TESS data agrees with the data from Diamond-Lowe et al. (2018) (see Figure 9). Nevertheless, while the data sets could potentially be compatible, we err on the side of caution and do not perform a joint fit. We note that the study by Diamond-Lowe et al. (2018) also concluded that GJ 1132b could not have a clear, primordial envelope, and thus the studies are in agreement on this conclusion. Additionally, the Spitzer transit from Dittmann et al. (2017) exhibits a similar transit depth to ours, but again we do not include it in a joint fit. Finally, we note that Southworth et al. (2017) claimed the detection of an atmosphere due to the modulation of several ground-based photometric measurements, but given that the precision obtained in Diamond-Lowe et al. (2018) was higher than in said study, we do not include it in our plots.

During the review process of this paper, an independent study also analyzed the same HST WFC3 data of GJ 1132b. Swain et al. (2021) found evidence for a slope over this wavelength region, attributed to an H_2-dominated atmosphere with hazes, as well as spectral features that were proposed to be due to absorption by CH_4 and HCN. Their work suggested that GJ 1132b had lost its primordial envelope and gained a second atmosphere through volcanic processes that released H_2 captured in an early age.

As our extracted spectrum differs greatly from that of Swain et al. (2021), we conducted an independent analysis of the data sets with an additional open-source pipeline: the Calibration of trAnsit Spectroscopy using CAusal Data (CASCADe[23]). While Iraclis has been developed specifically for analyzing HST

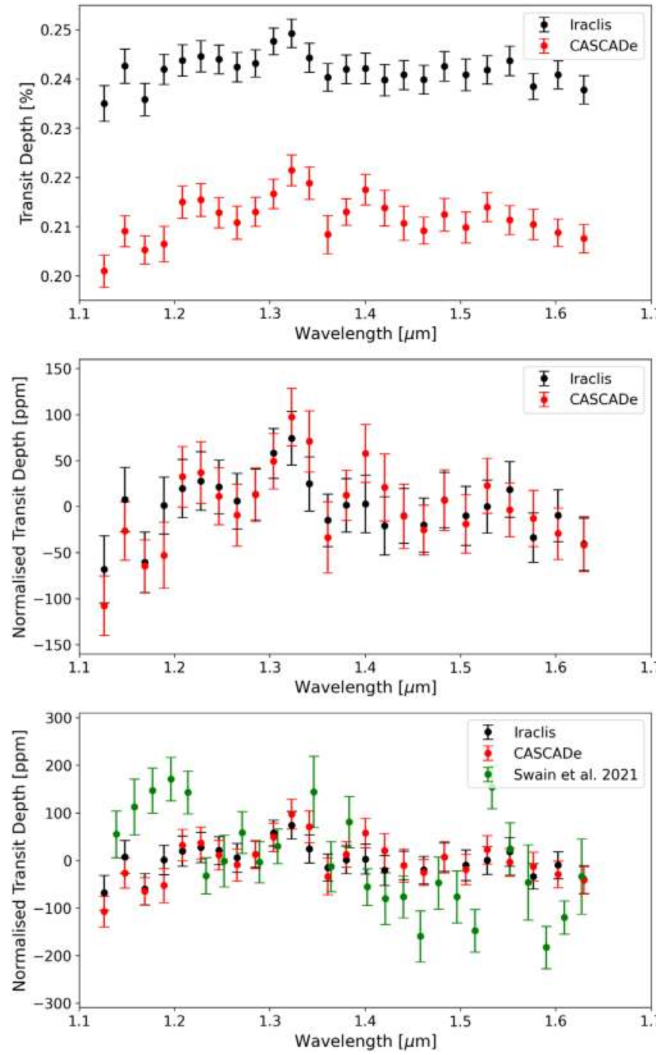

Figure 10. Comparison of the results from the data reduction and spectrum extraction undertaken here using Iraclis and CASCADe. While there is an offset between the spectra, normalizing them by their mean transit depth shows that they are consistent to within 1σ. However, the spectra recovered with both pipelines here differ significantly from those from Swain et al. (2021).

WFC3, CASCADe is an instrument-independent reduction pipeline and has been applied to both HST and Spitzer data sets. The CASCADe pipeline starts the data reduction with the ima intermediate data product, which was produced by the CALWFC3 data reduction pipeline (note that Iralcis takes the raw data and applies calibration steps itself). CASCADe implements a novel data-driven method, pioneered by Schölkopf et al. (2016), utilizing the causal connections within a data set to calibrate the spectral time-series data. For a full description of the pipeline steps, we refer the reader to Carone et al. (2021).

We ran CASCADe using the same planet parameters and limb-darkening coefficients as discussed in Section 2.1. A comparison between these spectra, and to those obtained by Swain et al. (2021), is given in Figure 10. We immediately notice a vertical offset in the spectra obtained by Iraclis and CASCADe. The offset is likely to be caused by differences in the correction of the systematics, and such offsets between different pipelines have been seen before, for example, for WASP-117 b (Anisman et al. 2020; Carone et al. 2021) and KELT-11 b (Changeat et al. 2020; Colón et al. 2020). The

[23] https://jbouwman.gitlab.io/CASCADe/

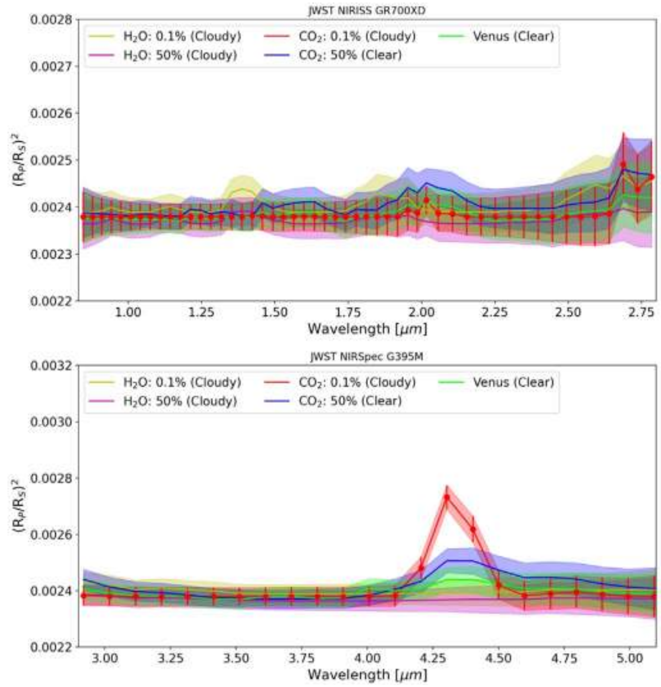

Figure 11. Simulated JWST observations for various atmospheric types that are consistent with current data. The colored regions show the 1σ errors on the observation that has been binned to $R \sim 50$.

finding of this offset provides further evidence that combining instruments without wavelength overlap is dangerous (Yip et al. 2020, 2021).

Despite this offset, we note that the spectral features in the CASCADe spectrum, or lack thereof, are highly similar to those obtained with Iraclis. By subtracting the mean from each spectrum, we show that the recovered data points are all within 1σ. Comparing these to Swain et al. (2021), we clearly highlight the disparity between our study and theirs: whereas they uncover spectral variations of ± 200 ppm from the mean transit depth, both our pipelines yield spectra where 21 of the 25 data points (84%) lie within ± 50 ppm of the mean transit depth, with no data points being more than 75 ppm from the mean.

The exact cause of the difference in the recovered transmission spectra between this study and that of Swain et al. (2021) is hard to discern without detailed one to one comparisons of the pipelines utilized. Iraclis and CASCADe are both open source, are well used, and have been validated against other results within the literature. Additionally, their approach to the data calibration and reduction, especially in the fitting of the systematic trends that are encountered within HST WFC3 data, is utterly different, and so achieving almost identical spectra with these pipelines leads us to have confidence in our results. Our team is working closely with those from Swain et al. (2021) to resolve the discrepancy between our work and theirs.

4.4. Future Missions

Future missions will offer increased sensitivity and wider spectral coverage. This will be key in the hunt for atmospheric features on smaller planets. While Ariel will be able to characterize H/He-dominated atmospheres (Edwards et al. 2019), or rule out their presence on small worlds, it may struggle to provide additional constraints on GJ 1132b given its lack of a clear H/He atmosphere and spectral features. Hence, we focus on JWST and show in Figure 11 the data that could be obtained from one single transit with either NIRISS GR700XD or NIRSpec G395M, modeled using ExoWebb, an adapted version of the Terminus tool described in Edwards & Stotesbury (2021) that uses the Pandeia engine (Pontoppidan et al. 2016). The colored regions show the 1σ errors on the observation that has been binned to $R \sim 50$, and as they can rarely be distinguished, this suggests that even JWST may struggle to disentangle different atmospheric types or provide significant evidence for molecular features. With the exception of the Venus-like case, the forward models assume an H/He envelope with the addition of the stated molecule. The cloud deck for the 0.1% H_2O and CO_2 atmospheres was set to 100 Pa (0.001 bar), while 10 Pa (0.0001 bar) was included for the 50% H_2O case.

5. Conclusion

We present the data analysis of five spectroscopic observations of GJ 1132b obtained with the G141 grism of the WFC3 on board HST. We extracted the planetary transmission spectra with Iraclis pipeline and attempted to retrieve the atmospheric composition using TauREx3. Our findings agree with those of Diamond-Lowe et al. (2018), and the transmission spectrum we obtain from our data shows no molecular features in the investigated wavelength range. We compared the spectrum with different atmospheric types to verify the noncompliance with any molecular content at the data precision, and we concluded that it is compatible with a flat transmission spectrum only. Future astronomical missions, such as JWST, will help further constrain the atmospheric properties of GJ 1132b, although multiple observations may be required for spectral features to be discerned. While it may be difficult to understand its true nature, GJ 1132b remains an interesting candidate for future atmospheric studies.

We thank our anonymous referee for the insightful comments which have improved the quality of our work. Additionally, we thank Mark Swain and his team for open and constructive talks surrounding the analysis of these data sets. This work was realized as part of "ARES Ariel School" in Biarritz in 2019. The school was organized by J.P.-B., A.T., and I.W. with the financial support of CNES. J.P.-B. acknowledges the support of the University of Tasmania through the UTAS Foundation and the endowed Warren Chair in Astronomy, Rodolphe Cledassou, Pascale Danto, and Michel Viso (CNES). W.P., T.Z., and A.Y.J. have received funding from the European Research Council (ERC) under the European Union's Horizon 2020 research and innovation program (grant agreement No. 679030/WHIPLASH and No. 758892/ExoAI). S.W. was supported through the STFC UCL CDT in Data Intensive Science (grant No. ST/P006736/1). L. V.M. and D.M.-G. acknowledge the financial support of the ARIEL ASI grant No. 2018-22-HH.0. B.E., Q.C., M.M., A.T., and I.W. acknowledge funding from the European Research Council (ERC) under the European Union's Horizon 2020 research and innovation program grant ExoAI (GA No. 758892) and the STFC grants ST/P000282/1, ST/P002153/1, ST/S002634/1, and ST/T001836/1. G.G. acknowledges the financial support of the 2017 PhD fellowship program of INAF. R.B. is a PhD fellow of the Research Foundation—Flanders (FWO). D.B. acknowledges financial support from the ANR project "e-PYTHEAS" (ANR-16-CE31-0005-01). N.S.

acknowledges the support of the IRIS-OCAV, PSL. M.P. acknowledges support by the European Research Council under Grant Agreement ATMO 757858 and by the CNES. O.V. thanks the CNRS/INSU Programme National de Planétologie (PNP) and CNES for funding support. J.B. acknowledges support from the European Research Council under the European Union's Horizon 2020 research and innovation program ExoplANETS-A (GA No. 776403). G.M. has received funding from the European Union's Horizon 2020 research and innovation program under the Marie Skłodowska-Curie grant agreement No. 895525.

Data: This work is based on observations with the NASA/ESA Hubble Space Telescope, obtained at the Space Telescope Science Institute (STScI) operated by AURA, Inc. The publicly available HST observations presented here were taken for proposal 14758, led by Zach Berta-Thompson (Berta-Thompson et al. 2016). These were obtained from the Hubble Archive, which is part of the Mikulski Archive for Space Telescopes. This paper also includes data collected by the TESS mission, which is funded by the NASA Explorer Program. TESS data are also publicly available via the Mikulski Archive for Space Telescopes (MAST).

Software: Iraclis (Tsiaras et al. 2016c), TauREx3 (Al-Refaie et al. 2019), pylightcurve (Tsiaras et al. 2016b), ExoTETHyS (Morello et al. 2020), Astropy (Astropy Collaboration et al. 2018), h5py (Collette 2013), emcee (Foreman-Mackey et al. 2013), Matplotlib (Hunter 2007), Multinest (Feroz et al. 2009; Buchner et al. 2014), Pandas (Reback et al. 2020), Numpy (Oliphant 2006), SciPy (Virtanen et al. 2020).

ORCID iDs

Lorenzo V. Mugnai https://orcid.org/0000-0002-9007-9802
Darius Modirrousta-Galian https://orcid.org/0000-0001-6425-9415
Billy Edwards https://orcid.org/0000-0002-5494-3237
Quentin Changeat https://orcid.org/0000-0001-6516-4493
Giuseppe Morello https://orcid.org/0000-0002-4262-5661
Ahmed Al-Refaie https://orcid.org/0000-0003-2241-5330
Michelle Fabienne Bieger https://orcid.org/0000-0001-9166-3042
Amélie Gressier https://orcid.org/0000-0003-0854-3002
Gloria Guilluy https://orcid.org/0000-0002-1259-2678
Mario Morvan https://orcid.org/0000-0001-8587-2112
William Pluriel https://orcid.org/0000-0001-7272-0363
Nour Skaf https://orcid.org/0000-0002-9372-5056
Kai Hou Yip https://orcid.org/0000-0002-9616-1524
Tiziano Zingales https://orcid.org/0000-0001-6880-5356
Benjamin Charnay https://orcid.org/0000-0003-0977-6545
Pierre Drossart https://orcid.org/0000-0001-7261-0228
Jérémy Leconte https://orcid.org/0000-0002-3555-480X
Olivia Venot https://orcid.org/0000-0003-2854-765X
Ingo Waldmann https://orcid.org/0000-0002-4205-5267
Jean-Philippe Beaulieu https://orcid.org/0000-0003-0014-3354

References

Abel, M., Frommhold, L., Li, X., & Hunt, K. L. C. 2011, JPCA, 115, 6805
Abel, M., Frommhold, L., Li, X., & Hunt, K. L. C. 2012, JChPh, 136, 044319
Adams, E. R., Seager, S., & Elkins-Tanton, L. 2008, ApJ, 673, 1160
Al-Refaie, A. F., Changeat, Q., Waldmann, I. P., & Tinetti, G. 2019, arXiv:1912.07759
Anisman, L. O., Edwards, B., Changeat, Q., et al. 2020, AJ, 160, 233
Astropy Collaboration, Price-Whelan, A. M., Sipőcz, B. M., et al. 2018, AJ, 156, 123
Barber, R. J., Strange, J. K., Hill, C., et al. 2014, MNRAS, 437, 1828
Barton, E. J., Hill, C., Yurchenko, S. N., et al. 2017, JQSRT, 187, 453
Benneke, B., Wong, I., Piaulet, C., et al. 2019, ApJL, 887, L14
Berta-Thompson, Z. K., Charbonneau, D., Diamond-Lowe, H., et al. 2016, The Hydrogen Content of a Rocky Earth-Size Exoplanet, HST Proposal 14758
Berta-Thompson, Z. K., Irwin, J., Charbonneau, D., et al. 2015, Natur, 527, 204
Bézard, B., Charnay, B., & Blain, D. 2020, arXiv:2011.10424
Blain, D., Charnay, B., & Bézard, B. 2021, A&A, 646, A15
Bonfils, X., Almenara, J. M., Cloutier, R., et al. 2018, A&A, 618, A142
Bruno, G., Lewis, N. K., Alam, M. K., et al. 2020, MNRAS, 491, 5361
Buchner, J., Georgakakis, A., Nandra, K., et al. 2014, A&A, 564, A125
Carone, L., Mollière, P., Zhou, Y., et al. 2021, A&A, 646, A168
Chachan, Y., & Stevenson, D. J. 2018, ApJ, 854, 21
Changeat, Q., & Edwards, B. 2021, ApJL, 907, L22
Changeat, Q., Edwards, B., Al-Refaie, A. F., et al. 2020, AJ, 160, 260
Christiansen, J. L., Vanderburg, A., Burt, J., et al. 2017, AJ, 154, 122
Claret, A. 2000, A&A, 363, 1081
Claret, A. 2018, A&A, 618, A20
Collette, A. 2013, Python and HDF5 (Sebastopol, CA: O'Reilly)
Colón, K. D., Kreidberg, L., Welbanks, L., et al. 2020, AJ, 160, 280
Dai, F., Masuda, K., Winn, J. N., & Zeng, L. 2019, ApJ, 883, 79
de Wit, J., Wakeford, H. R., Gillon, M., et al. 2016, Natur, 537, 69
Diamond-Lowe, H., Berta-Thompson, Z., Charbonneau, D., & Kempton, E. M. R. 2018, AJ, 156, 42
Dittmann, J. A., Irwin, J. M., Charbonneau, D., Berta-Thompson, Z. K., & Newton, E. R. 2017, AJ, 154, 142
Dorn, C., Harrison, J. H. D., Bonsor, A., & Hands, T. O. 2019, MNRAS, 484, 712
Dorn, C., Noack, L., & Rozel, A. B. 2018, A&A, 614, A18
Dorn, C., Venturini, J., Khan, A., et al. 2017, A&A, 597, A37
Edwards, B., Changeat, Q., Baeyens, R., et al. 2020a, AJ, 160, 8
Edwards, B., Changeat, Q., Mori, M., et al. 2021, AJ, 161, 44
Edwards, B., Changeat, Q., Yip, K. H., et al. 2020b, MNRAS, in press, (doi:10.1093/mnras/staa1245)
Edwards, B., Mugnai, L., Tinetti, G., Pascale, E., & Sarkar, S. 2019, AJ, 157, 242
Edwards, B., & Stotesbury, I. 2021, arXiv:2101.10317
Feroz, F., Hobson, M. P., & Bridges, M. 2009, MNRAS, 398, 1601
Feroz, F., Hobson, M. P., & Bridges, M. 2011, MultiNest: Efficient and Robust Bayesian Inference, Astrophysics Source Code Library, ascl:1109.006
Fletcher, L. N., Gustafsson, M., & Orton, G. S. 2018, ApJS, 235, 24
Foreman-Mackey, D., Hogg, D. W., Lang, D., & Goodman, J. 2013, PASP, 125, 306
Grimm, S. L., Demory, B.-O., Gillon, M., et al. 2018, A&A, 613, A68
Guilluy, G., Gressier, A., Wright, S., et al. 2021, AJ, 161, 19
Guo, X., Crossfield, I. J. M., Dragomir, D., et al. 2020, AJ, 159, 239
Hadden, S., & Lithwick, Y. 2014, ApJ, 787, 80
Harpsøe, K. B. W., Hardis, S., Hinse, T. C., et al. 2013, A&A, 549, A10
Hill, C., Yurchenko, S. N., & Tennyson, J. 2013, Icar, 226, 1673
Hunter, J. D. 2007, CSE, 9, 90
Ikoma, M., & Hori, Y. 2012, ApJ, 753, 66
Jespersen, C. K., & Stevenson, D. J. 2020, AAS Meeting Abstracts, 235, 174.07
Jindal, A., de Mooij, E. J. W., Jayawardhana, R., et al. 2020, AJ, 160, 101
Kite, E. S., Manga, M., & Gaidos, E. 2009, ApJ, 700, 1732
Kreidberg, L., Bean, J. L., Désert, J.-M., et al. 2014, Natur, 505, 69
Kreidberg, L., Koll, D. D. B., Morley, C., et al. 2019, Natur, 573, 87
Li, G., Gordon, I. E., Rothman, L. S., et al. 2015, ApJS, 216, 15
Luque, R., Pallé, E., Kossakowski, D., et al. 2019, A&A, 628, A39
Madhusudhan, N., Lee, K. K. M., & Mousis, O. 2012, ApJL, 759, L40
Marcy, G. W., Isaacson, H., Howard, A. W., et al. 2014, ApJS, 210, 20
Marley, M. S., Gelino, C., Stephens, D., Lunine, J. I., & Freedman, R. 1999, ApJ, 513, 879
Matsakos, T., Uribe, A., & Königl, A. 2015, A&A, 578, A6
Ment, K., Dittmann, J. A., Astudillo-Defru, N., et al. 2019, AJ, 157, 32
Mikal-Evans, T., Crossfield, I. J. M., Benneke, B., et al. 2021, AJ, 161, 18
Mocquet, A., Grasset, O., & Sotin, C. 2014, RSPTA, 372, 20130164
Modirrousta-Galian, D., Ito, Y., & Micela, G. 2021, Icar, 358, 114175
Modirrousta-Galian, D., Locci, D., Tinetti, G., & Micela, G. 2020a, ApJ, 888, 87
Modirrousta-Galian, D., Stelzer, B., Magaudda, E., et al. 2020b, A&A, 641, A113
Morello, G., Claret, A., Martin-Lagarde, M., et al. 2020, AJ, 159, 75

Morello, G., Tsiaras, A., Howarth, I. D., & Homeier, D. 2017, AJ, 154, 111
Mousis, O., Deleuil, M., Aguichine, A., et al. 2020, ApJL, 896, L22
Murgas, F., Chen, G., Nortmann, L., Pallé, E., & Nowak, G. 2020, A&A, 641, A158
Nayakshin, S., & Lodato, G. 2012, MNRAS, 426, 70
Noack, L., Rivoldini, A., & Van Hoolst, T. 2017, PEPI, 269, 40
Oliphant, T. E. 2006, A Guide to NumPy, Vol. 1 (Spanish Fork, UT: Trelgol Publishing)
Penz, T., & Micela, G. 2008, A&A, 479, 579
Pluriel, W., Whiteford, N., Edwards, B., et al. 2020, AJ, 160, 112
Polyansky, O. L., Kyuberis, A. A., Zobov, N. F., et al. 2018, MNRAS, 480, 2597
Pontoppidan, K. M., Pickering, T. E., Laidler, V. G., et al. 2016, Proc. SPIE, 9910, 991016
Quenouille, M. H. 1949, Ann. Math. Statist., 20, 355
Quenouille, M. H. 1956, Biometrika, 43, 353
Reback, J., McKinney, W., Mendel, B., et al. 2020, pandas-dev/pandas: Pandas 1.0.3, Zenodo, doi:10.5281/zenodo.3509134
Rice, K., Malavolta, L., Mayo, A., et al. 2019, MNRAS, 484, 3731
Rocchetto, M., Waldmann, I. P., Venot, O., Lagage, P.-O., & Tinetti, G. 2016, ApJ, 833, 120
Rothman, L. S., Gamache, R. R., Goldman, A., et al. 1987, ApOpt, 26, 4058
Rothman, L. S., Gordon, I. E., Barber, R. J., et al. 2010, JQSRT, 111, 2139
Sanz-Forcada, J., Micela, G., Ribas, I., et al. 2011, A&A, 532, A6
Schlawin, E., Leisenring, J., McElwain, M. W., et al. 2021, AJ, 161, 115
Schölkopf, B., Hogg, D. W., Wang, D., et al. 2016, PNAS, 113, 7391
Skaf, N., Bieger, M. F., Edwards, B., et al. 2020, AJ, 160, 109
Smith, J. C., Stumpe, M. C., Van Cleve, J. E., et al. 2012, PASP, 124, 1000
Southworth, J., Mancini, L., Madhusudhan, N., et al. 2017, AJ, 153, 191
Stevenson, K. B., Bean, J. L., Fabrycky, D., & Kreidberg, L. 2014a, ApJ, 796, 32
Stevenson, K. B., Bean, J. L., Seifahrt, A., et al. 2014b, AJ, 147, 161
Stumpe, M. C., Smith, J. C., Catanzarite, J. H., et al. 2014, PASP, 126, 100
Stumpe, M. C., Smith, J. C., Van Cleve, J. E., et al. 2012, PASP, 124, 985
Swain, M. R., Estrela, R., Roudier, G. M., et al. 2021, AJ, 161, 213
Tennyson, J., Yurchenko, S. N., Al-Refaie, A. F., et al. 2016, JMoSp, 327, 73
Tsiaras, A., Rocchetto, M., Waldmann, I. P., et al. 2016a, ApJ, 820, 99
Tsiaras, A., Waldmann, I., Rocchetto, M., et al. 2016b, pylightcurve: Exoplanet lightcurve model, Astrophysics Source Code Library, ascl:1612.018
Tsiaras, A., Waldmann, I. P., Rocchetto, M., et al. 2016c, ApJ, 832, 202
Tsiaras, A., Waldmann, I. P., Tinetti, G., Tennyson, J., & Yurchenko, S. N. 2019, NatAs, 3, 1086
Tsiaras, A., Waldmann, I. P., Zingales, T., et al. 2018, AJ, 155, 156
Tukey, J. W. 1958, Ann. Math. Statist., 29, 614
Valencia, D., Guillot, T., Parmentier, V., & Freedman, R. S. 2013, ApJ, 775, 10
Van Grootel, V., Gillon, M., Valencia, D., et al. 2014, ApJ, 786, 2
Virtanen, P., Gommers, R., Oliphant, T. E., et al. 2020, NatMe, 17, 261
Waldmann, I. P., Rocchetto, M., Tinetti, G., et al. 2015a, ApJ, 813, 13
Waldmann, I. P., Tinetti, G., Rocchetto, M., et al. 2015b, ApJ, 802, 107
Western, C. M., Carter-Blatchford, L., Crozet, P., et al. 2018, JQSRT, 219, 127
Yip, K. H., Changeat, Q., Edwards, B., et al. 2021, AJ, 161, 4
Yip, K. H., Tsiaras, A., Waldmann, I. P., & Tinetti, G. 2020, AJ, 160, 171
Yurchenko, S. N., Barber, R. J., & Tennyson, J. 2011, MNRAS, 413, 1828
Yurchenko, S. N., & Tennyson, J. 2014, MNRAS, 440, 1649
Zeng, L., & Sasselov, D. 2013, PASP, 125, 227
Zeng, L., Sasselov, D. D., & Jacobsen, S. B. 2016, ApJ, 819, 127
Zhang, M., Knutson, H. A., Wang, L., et al. 2021, AJ, 161, 181
Zilinskas, M., Miguel, Y., Lyu, Y., & Bax, M. 2021, MNRAS, 500, 2197